RSC Advances

PAPER

View Article Online
View Journal | View Issue

Cite this: *RSC Adv.*, 2023, **13**, 31112

Bluish-green afterglow and blue photoluminescence of undoped $BaAl_2O_4$

Bao-Gai Zhai and Yuan Ming Huang *

Received 4th August 2023
Accepted 18th October 2023

DOI: 10.1039/d3ra05294j

rsc.li/rsc-advances

Undoped $BaAl_2O_4$ was derived *via* sol–gel combustion technique. The afterglow and photoluminescence (PL) properties of undoped $BaAl_2O_4$ were explored with the combination of experiments and density functional theory (DFT) calculations. Undoped $BaAl_2O_4$ is found to display bluish-green afterglow that is discernible to naked eye in dark for about 20 s. The broad afterglow spectrum of undoped $BaAl_2O_4$ is peaked at around 495 nm. As a contrast, the broad PL spectrum of undoped $BaAl_2O_4$ can be decomposed into a bluish-green PL band peaking at about 2.53 eV (490 nm) and a blue PL band centered at about 3.08 eV (402.6 nm). DFT calculations indicate that the defect energy levels generated by oxygen and barium vacancies are critical to the afterglow and PL of undoped $BaAl_2O_4$. This work demonstrates that the oxygen and barium vacancies in undoped $BaAl_2O_4$ are liable for the bluish-green afterglow and blue PL of undoped $BaAl_2O_4$. The recorded bluish-green afterglow of $BaAl_2O_4$ is particularly important to understand the afterglow mechanisms of rare-earth doped $BaAl_2O_4$.

1. Introduction

Upon the stimulation of the green afterglow of Eu^{2+} and Dy^{3+} codoped $SrAl_2O_4$,[1] both the afterglow and the photoluminescence (PL) of rare-earth doped $BaAl_2O_4$ have been intensively investigated.[2–6] It is documented that Eu^{2+} and Re^{3+} codoped $BaAl_2O_4$ ($BaAl_2O_4$:Eu^{2+},Re^{3+}) phosphors display bluish-green afterglows with their emission maxima located at around 490–500 nm where Re represents an auxiliary rare-earth dopant.[2,5,6] Additionally, Dy^{3+} singly doped $BaAl_2O_4$ exhibits quite similar bluish-green afterglow.[7] Besides their afterglows, $BaAl_2O_4$:Eu^{2+},Re^{3+} phosphors also give off bluish-green PL peaking at about 500 nm as Re = Dy,[2–5,8–10] Nd, Gd, Sm, Ce, Er, Pr, Tb.[4] Irrespective of the difference in Re, the PL spectra of $BaAl_2O_4$:Eu^{2+},Re^{3+} are similar to that of Eu^{2+} doped $BaAl_2O_4$ ($BaAl_2O_4$:Eu^{2+}).[11–14] Consequently, Eu^{2+} is generally assumed to be the luminescent center of afterglow and the luminescent center of PL for $BaAl_2O_4$:Eu^{2+} and $BaAl_2O_4$:Eu^{2+},Re^{3+}.[1–18]

This belief is, however, challenged by a number of theoretical and experimental results: (i) both undoped $SrAl_2O_4$ and Eu^{2+} doped $SrAl_2O_4$ exhibit quite similar green afterglow;[19] (ii) both undoped $CaAl_2O_4$ and Eu^{2+} doped $CaAl_2O_4$ exhibit quite similar blue afterglow;[20,21] (iii) the peak of the afterglow spectrum of Eu^{2+} doped $CaAl_2O_4$ does not shift regardless the variation in doping concentration;[22] (iv) the green afterglow of Dy^{3+} doped $SrAl_2O_4$ and Tb^{3+} doped $SrAl_2O_4$ is quite similar to the afterglow of Eu^{2+} doped $SrAl_2O_4$;[23–26] (v) Dy^{3+} doped $BaAl_2O_4$ exhibits bluish-green afterglow which is quite similar to that of $BaAl_2O_4$:Eu^{2+};[7] (vi) density functional theory (DFT) calculations demonstrate that the afterglows of undoped $SrAl_2O_4$, undoped $CaAl_2O_4$ and Eu^{2+} doped $SrAl_2O_4$ originate from oxygen vacancy and cation vacancy in the hosts;[19–21,27] (vii) oxygen vacancies are held responsible for the afterglows of a number of undoped inorganic materials such as HfO_2,[28] $SrAl_2O_4$,[19] $CaAl_2O_4$,[20,21] $SrSO_4$,[29] boric oxide,[30] and ZrO_2.[31] These challenging facts suggest that the afterglow and PL properties of undoped $BaAl_2O_4$ are critically important for us to comprehensively unveil the afterglow mechanisms of $BaAl_2O_4$:Eu^{2+},Re^{3+}. In other words, undoped $BaAl_2O_4$ would exhibit bluish-green afterglow if intrinsic defects in $BaAl_2O_4$ were liable for the afterglows of $BaAl_2O_4$:Eu^{2+} and $BaAl_2O_4$:Eu^{2+},Re^{3+}. In this paper, bluish-green afterglow and blue PL of undoped $BaAl_2O_4$ are reported. Bluish-green afterglow of undoped $BaAl_2O_4$ is discernible to naked eye in dark for about 20 s. The broad afterglow spectrum of undoped $BaAl_2O_4$ is peaked at about 495 nm. DFT calculations show that oxygen and barium vacancies in $BaAl_2O_4$ introduce midgap states. The thermoluminescence (TL) glow curve is given. The oxygen and barium vacancies in $BaAl_2O_4$ are demonstrated to be the luminescence center of afterglow for undoped $BaAl_2O_4$.

2. Materials and methods

2.1. Preparation of undoped $BaAl_2O_4$

We employed the sol–gel combustion technique to prepare undoped $BaAl_2O_4$ phosphors.[7,32,33] Analytical grade reagents $Al(NO_3)_3 \cdot 9H_2O$), $Ba(NO_3)_2$, H_3BO_3 and urea were purchased from local chemical suppliers, *i.e.*, the Sinopharm Chemical Reagents Co., Ltd. The purity of each analytical reagent was 99.5% or higher. Theoretically speaking, absolutely pure

School of Microelectronics and Control Engineering, Changzhou University, Changzhou 213164, China. E-mail: dongshanisland@126.com

reagents with the purity of 100% are ideal starting materials to synthesize truly undoped $BaAl_2O_4$, but they are not practically available on the market. To minimize the possibility of unintentional doping, new alumina crucibles were used as the reaction vessels. Details on the solution preparation and sol–gel combustion can be found elsewhere.[20–22] After the sol–gel combustion, white powders were obtained. Subsequent annealing was performed at 700 °C for 3 h to assure the complete reactions of the raw materials. An attempt was made to analyze the resultant powders for trace contaminants. The resultant powders were tested for impurities using inductively coupled plasma mass spectrometry, but ultra-trace impurities of Eu^{2+}, Tb^{3+} and Dy^{3+} were not detected at ppm levels in the resultant powders. For brevity, the resultant products were denoted as undoped $BaAl_2O_4$.

2.2. Phase, morphology and PL spectra of $BaAl_2O_4$

The X-ray diffractometer (D/max 2500 PC, Rigaku Corporation) was employed to measure the X-ray diffraction (XRD) curve of undoped $BaAl_2O_4$. The energy dispersive X-ray (EDX) spectrum and the morphology of undoped $BaAl_2O_4$ were analyzed on the Hitachi scanning electron microscope (SEM). Micrographs of $BaAl_2O_4$ nanocrystals and their selected area electron diffraction pattern were analyzed with a transmission electron microscope (TEM) (JEOL JEM-2100, Japan Electronics Corp). To evaluate the binding energies of elements in undoped $BaAl_2O_4$, the X-ray photoelectron spectroscopy (XPS) spectra were measured on the Escalab 250Xi spectrophotometer (Thermo Scientific). Details on each instrument are available elsewhere.[22]

Upon the 325 nm radiation of a He–Cd laser, steady-state PL spectra of undoped $BaAl_2O_4$ were recorded with a spectrophotometer (Tianjin Gangdong Ltd., China). The PL decay curves of undoped $BaAl_2O_4$ were analyzed on a PL lifetime spectrometer (LifeSpec II, Edinburgh Instruments). The excitation wavelength, typical pulse width, and pulse repetition rate of the light source were 320 nm, 860 ps, and 10 MHz, respectively. Details on the characterization are available elsewhere.[34,35]

2.3. Afterglow spectrum, afterglow decay and TL glow curve of undoped $BaAl_2O_4$

With the spectrophotometer made by Tianjin Gangdong Ltd., the afterglow spectrum of undoped $BaAl_2O_4$ was analyzed after the ultraviolet excitation of a high-pressure Hg lamp (175 W) was terminated. The afterglow decay curve of undoped $BaAl_2O_4$ was taken by focusing the afterglows into the entrance slit of the spectrometer. The duration of the ultraviolet excitation from the high-pressure Hg lamp was 3 min. The TL glow curve of undoped $BaAl_2O_4$ was measured on a TL meter constructed according to the scheme given by Yamashita *et al.*[36] In order to create carriers to fill the traps in undoped $BaAl_2O_4$, the phosphors were irradiated under a low-pressure Hg lamp (254 nm, 32 W) for 5 min before TL data acquisition. The temperature rising rate was 2 K s^{-1}. Details on the TL glow curve measurement could be found elsewhere.[19,22,32,33,37]

2.4. Electronic structures of defective $BaAl_2O_4$

The band structures and the density of states (DOS) of oxygen-deficient $BaAl_2O_4$ and barium-deficient $BaAl_2O_4$ were calculated using the DFT module of Quantumwise Atomistix ToolKit 11.8 package. The exchange–correlation functional was described by the meta generalized gradient approximation, *i.e.*, the TB09LDA potential.[38–40] Instead of a supercell, one single unit cell was used for the DFT calculations. Consisting of 32 oxygen sites, 8 barium sites and 16 aluminum sites, the total number of ions in the unit cell of $BaAl_2O_4$ is 56. The lattice parameters of hexagonal $BaAl_2O_4$ were taken from Inorganic Crystal Structure Database with $a = 1.0447$ nm, $c = 0.8794$ nm (#75426). Oxygen-deficient $BaAl_2O_4$ was resulted when one oxygen site was vacant. The resultant $BaAl_2O_4$ was denoted as $BaAl_2O_{4-\delta}$ where $\delta = 0.125$. Similarly, barium-deficient $BaAl_2O_4$ was obtained when one barium site was vacant. The resultant $BaAl_2O_4$ was denoted as $Ba_{1-\delta}Al_2O_4$ where $\delta = 0.125$. The cut-off energy for the plane waves was 75 Hartree. The convergence criterion was 4×10^{-5} eV of total energy. The Monkhorst–Pack scheme *k*-points grid sampling was $5 \times 5 \times 5$ for the Brillouin zone. Details on the DFT calculations were available elsewhere.[41–43]

3. Results and discussions

3.1. Phase and morphology of $BaAl_2O_4$

Fig. 1(a) represents the XRD profile of undoped $BaAl_2O_4$. The diffraction peaks are located at 19.60, 21.84, 28.28, 34.32, 40.10, 41.13, 45.10, 45.84, 53.63, 54.55, 57.79, 61.59, 67.23, 69.74, and 74.36°. The standard diffractograms of hexagonal $BaAl_2O_4$, which are registered in the Joint Committee on Powder Diffraction Standards (JCPDS) as card no. 17-0306, are shown at the bottom of Fig. 1(a) for the purpose of comparison. A comparison of the data in Fig. 1(a) reveals that the XRD profile matches well with those of the standard hexagonal $BaAl_2O_4$ ($a = 1.0447$ nm, $c = 0.8794$ nm). The above listed diffraction peaks are assigned to the Bragg reflections from crystallographic planes (200), (201), (202), (220), (222), (004), (402), (204), (420), (224), (422), (600), (206), (424), and (226) of hexagonal $BaAl_2O_4$, respectively. Apparently, the XRD profile in Fig. 1(a) is consistent to those of $BaAl_2O_4$:Eu^{2+},Re^{3+}.[2,3,6–10] Consequently, the XRD pattern in Fig. 1(a) demonstrates that crystalline $BaAl_2O_4$ is resulted *via* the sol–gel combustion technique. Fig. 1(b) represents the Rietveld refinement of the XRD profile. The pseudo-Voigt function was used as peak shape function. The agreement factors of the Rietveld refinement are $R_p = 18.6\%$, $R_{wp} = 17.8\%$, $R_{exp} = 5.33\%$ and $\chi^2 = 11.1$. The Rietveld refinement reveals that the lattice constants of the unit cell of undoped $BaAl_2O_4$ are $a = 1.0440$ nm and $c = 0.8789$ nm, which are very close to those of the reference hexagonal $BaAl_2O_4$. The hexagonal $BaAl_2O_4$ has channels along its *c*-direction.[41]

Fig. 2 illustrates the morphology and microstructures of undoped $BaAl_2O_4$. As shown by the SEM micrograph in Fig. 2(a), undoped $BaAl_2O_4$ phosphors are prone to forming aggregates with irregular shapes.[4,7,12,14] The typical dimension of the

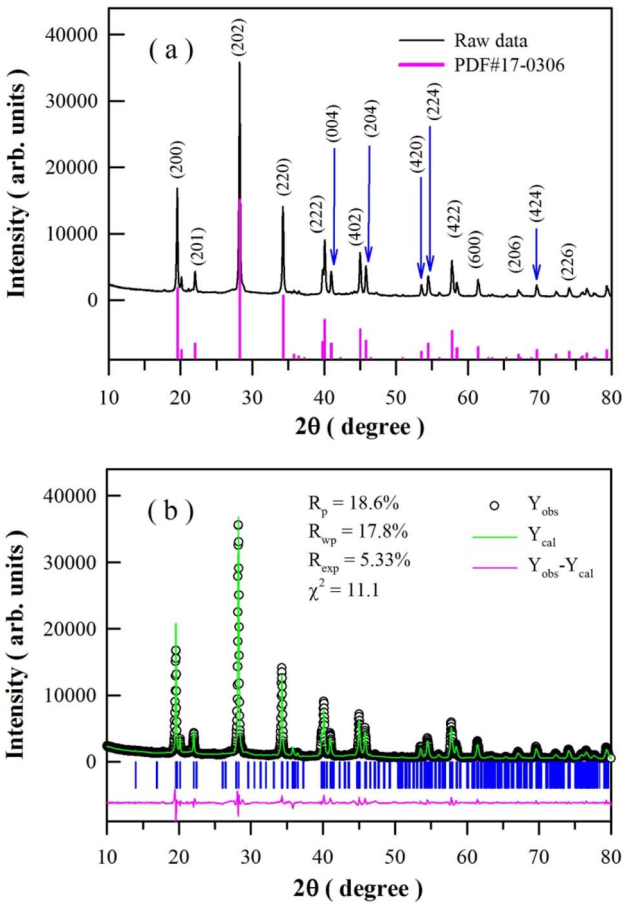

Fig. 1 (a) XRD profile of undoped $BaAl_2O_4$ and the standard diffractograms of hexagonal $BaAl_2O_4$ (JCPDF no. 17-0306). (b) XRD pattern of undoped $BaAl_2O_4$ and its Rietveld refinement. Solid green curve: Rietveld diffractogram. Open circles: raw data. Solid pink curve: residue.

aggregates is around 10 μm. Obviously, each aggregate is featured of a large number of pores which are distributed non-uniformly across the aggregate. The cross section of an aggregate of undoped $BaAl_2O_4$, as evidenced in Fig. 2(b), verifies the pore distribution in the aggregate. The typical dimension of the pores is around 0.5 μm. As documented in the literature, the formation of irregular aggregates with a large number of pores in them is the characteristics of sol–gel combustion derived $SrAl_2O_4$,[19,23–26] $CaAl_2O_4$,[20–22,32,33] and $BaAl_2O_4$.[7] Additionally, channels across the aggregates are identified in Dy^{3+} doped $CaAl_2O_4$ derived *via* sol–gel combustion.[37] As shown by the TEM micrograph of an aggregate in Fig. 2(c), the aggregate consists of a large number of randomly distributed nanocrystals, indicating the polycrystalline nature of the undoped $BaAl_2O_4$. Actually, nanocrystals are present in aggregates of sol–gel combustion derived $SrAl_2O_4$,[19,24,26] $CaAl_2O_4$,[20–22,32,33,37] and $BaAl_2O_4$.[7] The selected area electron diffraction pattern of undoped $BaAl_2O_4$ is displayed in Fig. 2(d). Indeed, the electron diffraction pattern verifies the polycrystalline nature of undoped $BaAl_2O_4$.

3.2. EDX spectrum and elemental mapping of undoped $BaAl_2O_4$

Fig. 3 illustrates the EDX spectrum of undoped $BaAl_2O_4$. It is clear that the characteristic X-ray emissions of O(Kα), Al(Kα), Au($M\alpha_1$), Ba($L\alpha_{1,2}$), Ba($L\beta_1$), Ba($L\beta_{2,15}$), Ba($L\gamma_1$) and Au($L\alpha_1$) are located at 0.525, 1.486, 2.122, 4.466, 4.828, 5.157, 5.531 and 9.713 keV, respectively. Au sputtering for SEM analysis is responsible for the presence of Au in the sample.[19,22,37] Therefore, Fig. 3 verifies the presence of Al, Ba and O in the synthesized product.

Fig. 4 depicts the EDX elemental mappings of Ba, Al and O in undoped $BaAl_2O_4$. The electronic image of the selected area for elemental analysis is shown in Fig. 4(a). Fig. 4(b–d) represents the O map, Al map, and Ba map. The images in Fig. 4 reveal the uniform distribution across the sample of each element in undoped $BaAl_2O_4$.

3.3. XPS spectrum of undoped $BaAl_2O_4$

Fig. 5 depicts the survey scan (a) and high-resolution XPS spectra of Ba 3d (b), Al 2p (c) and O 1s (d) in undoped $BaAl_2O_4$. Fig. 5(a) shows that the peaks of Ba, Al, and O are present in the survey scan. Fig. 5(b) shows that the binding energies of Ba $3d_{5/2}$ and Ba $3d_{3/2}$ are 779.78 and 795.08 eV for undoped $BaAl_2O_4$, respectively. It is clear in Fig. 5(c) and (d) that the binding energies of Al $2p_{3/2}$ and O 1s are 73.88 and 531.55 eV for undoped $BaAl_2O_4$. For Ce^{3+} doped $BaAl_2O_4$ at the concentration of 3%, Chatterjee *et al.* reported that the binding energies of Ba $3d_{5/2}$, Ba $3d_{3/2}$, O 1s and Al $2p_{3/2}$ are 779.60, 795.60, 530.60 and 73.10 eV, respectively.[44] Our previous studies show that the peaks of the binding energies of Ba $3d_{5/2}$, Ba $3d_{3/2}$, and O 1s are approximately 780.0, 795.2 and 531.8 eV, respectively, for Dy^{3+} doped $BaAl_2O_4$ (4 mol%).[7] Obviously, the binding energies of O 1s, Al $2p_{3/2}$, Ba $3d_{5/2}$ and Ba $3d_{3/2}$ in undoped $BaAl_2O_4$ are close to those in Ce^{3+} doped $BaAl_2O_4$ and Dy^{3+} doped $BaAl_2O_4$.

3.4. Steady-state PL spectrum of undoped $BaAl_2O_4$

Fig. 6(a) represents the steady-state PL spectrum of undoped $BaAl_2O_4$ in wavelength scale. The inset in Fig. 6(a) represents the emission photo of undoped $BaAl_2O_4$ upon the 325 nm excitation. Apparently, this PL spectrum consists of more than one PL band due to its broad and asymmetric profile. To provide better physical insight, the PL spectrum in Fig. 6(a) is converted into a PL spectrum in energy scale by employing the Jacobian transformation.[45,46] Fig. 6(b) depicts the resultant PL spectrum in energy scale, which can be deconvoluted into one green PL band peaking at 2.53 eV (490.1 nm) and one blue PL band centering at 3.08 eV (402.6 nm). Obviously, the perception color of the emissions of undoped $BaAl_2O_4$ is blue. On the basis of the PL spectrum, the chromaticity coordinates of the PL are derived to be (0.1673, 0.1569) for undoped $BaAl_2O_4$.[47–49] The bandgap of $BaAl_2O_4$ is reported to be 6.47 eV.[50] Band-edge emission of $BaAl_2O_4$ can be ruled out because the photon energy of the 325 nm excitation of the laser beam (3.82 eV) is insufficient. Thus, the broadband PL spectra in Fig. 6 should originate from defect related emissions of $BaAl_2O_4$. Oxygen and barium

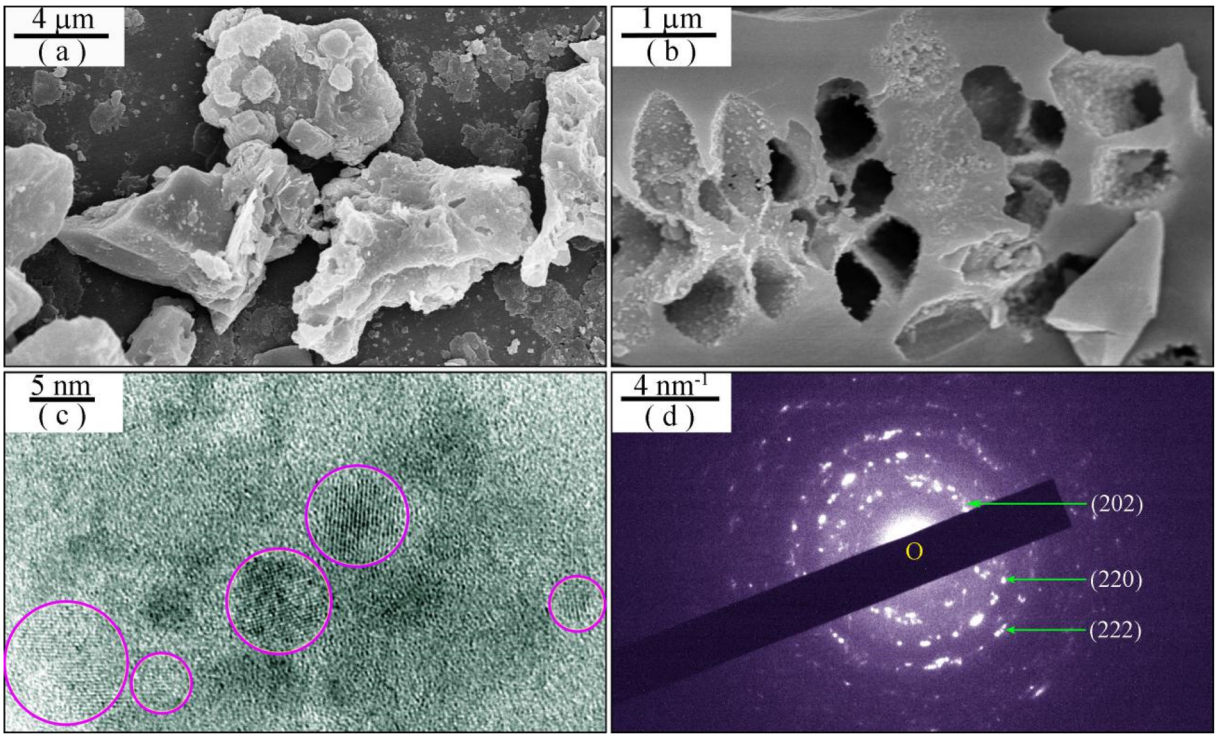

Fig. 2 Morphology and microstructures of undoped $BaAl_2O_4$: (a) SEM micrograph of aggregates; (b) SEM micrograph of the cross section of an aggregate; (c) TEM micrograph of one $BaAl_2O_4$ aggregate; and (d) selected area electron diffraction pattern of undoped $BaAl_2O_4$.

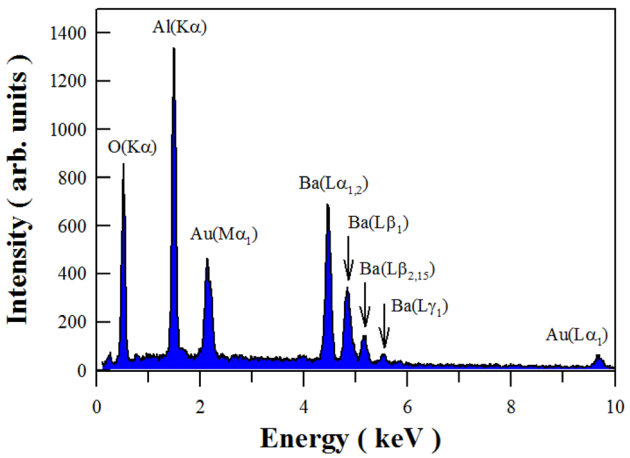

Fig. 3 EDX spectrum of undoped $BaAl_2O_4$.

vacancies are well known to be the most common defects in $BaAl_2O_4$. After considering the oxygen vacancy and cation vacancy related emissions in $SrAl_2O_4$,[19,24–26] $CaAl_2O_4$,[20–22,46] $BaAl_2O_4$,[7] $SrSO_4$,[29,51] HfO_2,[52] $ZnWO_4$,[53] and $ZnMoO_4$,[54,55] we tend to hold the oxygen and barium vacancies in $BaAl_2O_4$ liable for the two PL bands in Fig. 6(b). It is worthy of being noted that the PL intensities of Fig. 6(a) and (b) differ. To properly convert data recorded in units of wavelength, the signal values must be scaled by the Jacobian transformation. That is to say, the photon flux per constant interval of energy E in Fig. 6(b) is equal to the photon flux per constant interval of wavelength λ in Fig. 6(a) after scaled by a factor of hc/E^2.[45,46] The scale factor is responsible for the difference in the PL intensities of Fig. 6(a) and (b).

$BaAl_2O_4$:Eu^{2+} and $BaAl_2O_4$:Eu^{2+},Dy^{3+} are known to exhibit bluish-green PL with its dominant peak at about 490 nm (2.53 eV).[3–6,10] For instance, the room temperature PL spectrum of $BaAl_2O_4$:Eu^{2+},Dy^{3+} is peaked at 490 nm,[6] the broadband PL spectrum of $BaAl_2O_4$:Eu^{2+},Re^{3+} (Re = Dy, Nd, Gd, Sm, Ce, Er, Pr, Tb) is peaked at 500 nm.[4] Beside the dominant PL band varying in the range of 490–500 nm, a weak PL band often peaks at around 435 nm. For example, Rodrigues *et al.* and Stefani *et al.* reported that the PL spectrum for $BaAl_2O_4$:Eu^{2+},Dy^{3+} contains two PL bands, in which the dominant PL band is peaked at about 500 nm while the weak PL band is peaked at around 435 nm.[2,8] In our case, the steady-state PL spectra of $BaAl_2O_4$:-Eu^{2+} with the doping concentrations of 1 and 4 mol% demonstrate that, for each doping concentration, the dominant PL band is located at about 495 nm whilst the minor PL band is peaked at around 410 nm, as shown in Fig. 6(c) and (d). A comparison of the data reveals that the peak energies of the two PL bands of $BaAl_2O_4$:Eu^{2+} coincide with those of undoped $BaAl_2O_4$.

3.5. Afterglow spectrum and decay profile of undoped $BaAl_2O_4$

Undoped $BaAl_2O_4$ exhibits bluish-green afterglow after the ultraviolet excitation is ceased. The 3 min-long ultraviolet excitation is provided by a high-pressure mercury lamp. The afterglow last for about 20 s to naked eye in dark. The afterglow

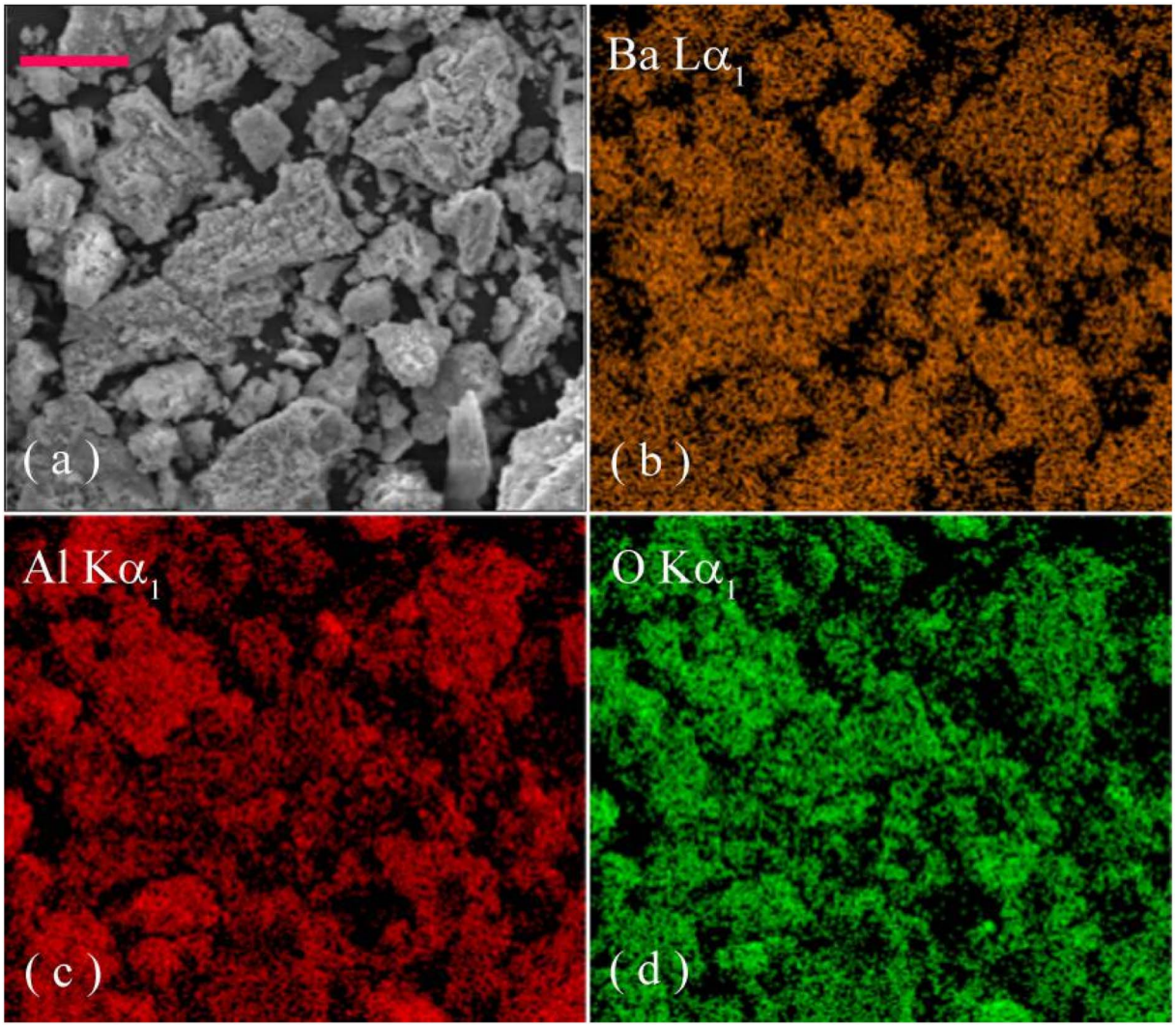

Fig. 4 Electronic image of a selected area (a) and elemental maps of Al (b), Ba (c) and O (d) in undoped $BaAl_2O_4$. The scale bar represents 30 μm.

spectrum of $BaAl_2O_4$ is illustrated in Fig. 7(a). Clearly, this broadband afterglow spectrum is peaked at about 495 nm. Both the profile and the peak position of this afterglow spectrum are quite similar to those of $BaAl_2O_4$:Eu^{2+},Dy^{3+}.[2,5,6] The insets in Fig. 7(a) show the photograph of undoped $BaAl_2O_4$ under lab illumination (left) and the afterglow photograph of the undoped $BaAl_2O_4$ (right). With the chromaticity coordinates of (0.1658, 0.3269), the bluish-green afterglow of undoped $BaAl_2O_4$ confirms the fact that intrinsic defects in $BaAl_2O_4$ are the origin of the afterglow.

The duration of afterglow is the time for which an afterglow material continues to glow after the cessation of excitation until its luminance drops to the threshold of 0.32 mcd m^{-2}. Fig. 7(b) represents the afterglow decay of undoped $BaAl_2O_4$. As shown by the red solid line, the raw data in Fig. 7(b) are fitted to a tri-exponential function. Clearly, undoped $BaAl_2O_4$ has three different decay components with constants of $\tau_1 = 0.0211$ s, $\tau_2 = 1.1138$ s and $\tau_3 = 8.9928$ s, which suggests a set of traps are present in the phosphor. According to the tri-exponential function, it takes about 24.7 s for the afterglow of undoped $BaAl_2O_4$ to drop to 0.32 mcd m^{-2}. Therefore, the afterglow duration of undoped $BaAl_2O_4$ is 24.7 s, which is very close to that estimated with naked eye in dark.

We compared the afterglow intensity of the undoped $BaAl_2O_4$ with those of Eu^{2+} doped $BaAl_2O_4$ (1 and 4 mol%) to see whether the afterglow intensity is independent on the doping level. For undoped $BaAl_2O_4$ without subsequent treatments, its afterglow intensity is about one tenth of those of Eu^{2+} doped $BaAl_2O_4$ (1 and 4 mol%). After annealing in oxygen poor environment, however, the afterglow intensity of undoped $BaAl_2O_4$ can be stronger than the afterglow intensity of Eu^{2+} doped $BaAl_2O_4$ (1 and 4 mol%). These data indicate that the afterglow intensities of both the undoped $BaAl_2O_4$ and Eu^{2+} doped $BaAl_2O_4$ (1 and 4 mol%) are independent on the doping level.

3.6. TL glow curve of undoped $BaAl_2O_4$

The TL glow curve of undoped $BaAl_2O_4$ is depicted in Fig. 8. Peaking at around 313.8 K (40.7 °C), this broad TL glow curve

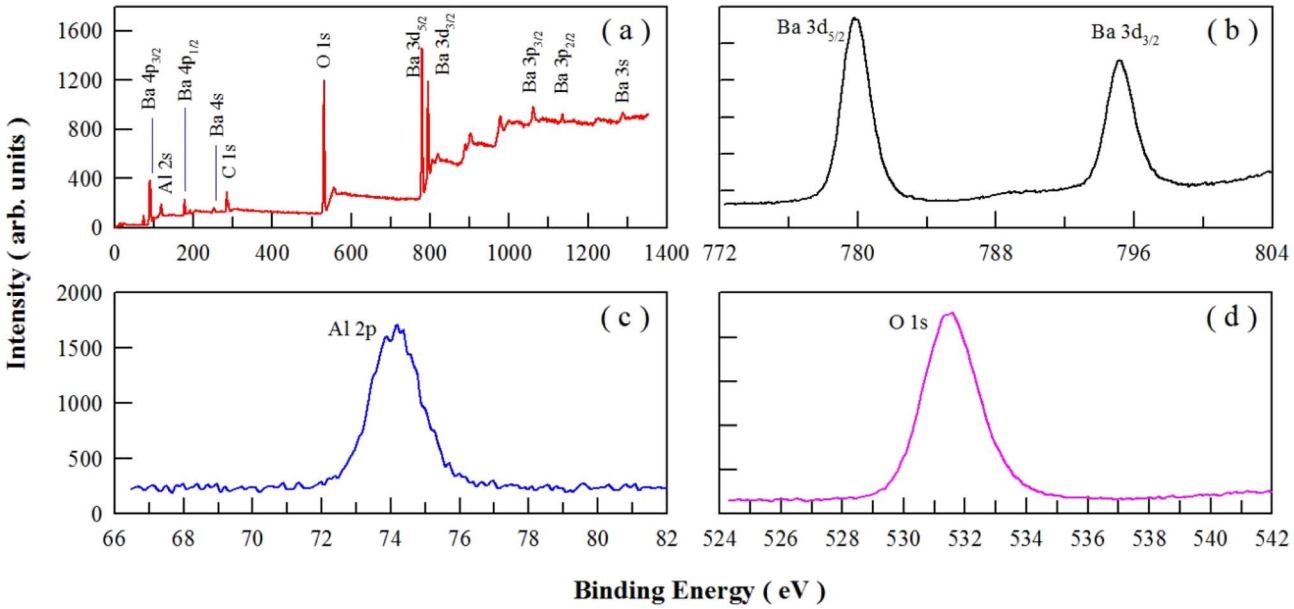

Fig. 5 Survey scan (a) and high-resolution XPS spectra of Ba 3d (b), Al 2p (c) and O 1s (d) in undoped $BaAl_2O_4$.

means that multiple trap levels are present in $BaAl_2O_4$.[56] Rodrigues *et al.* and Lephoto *et al.* recorded the TL glow curves of $BaAl_2O_4$:Eu^{2+},Re^{3+} (Re = La, Ce, Pr, Nd, Sm, Dy, Gd, Tb, Er, Tm);[2,4,50] Aizawa *et al.* recorded the TL glow curve of $BaAl_2O_4$:-Eu^{2+},Dy^{3+} films,[10] Pandey and Chithambo displayed the TL glow curve of electron irradiated $BaAl_2O_4$.[57] Obviously, both the

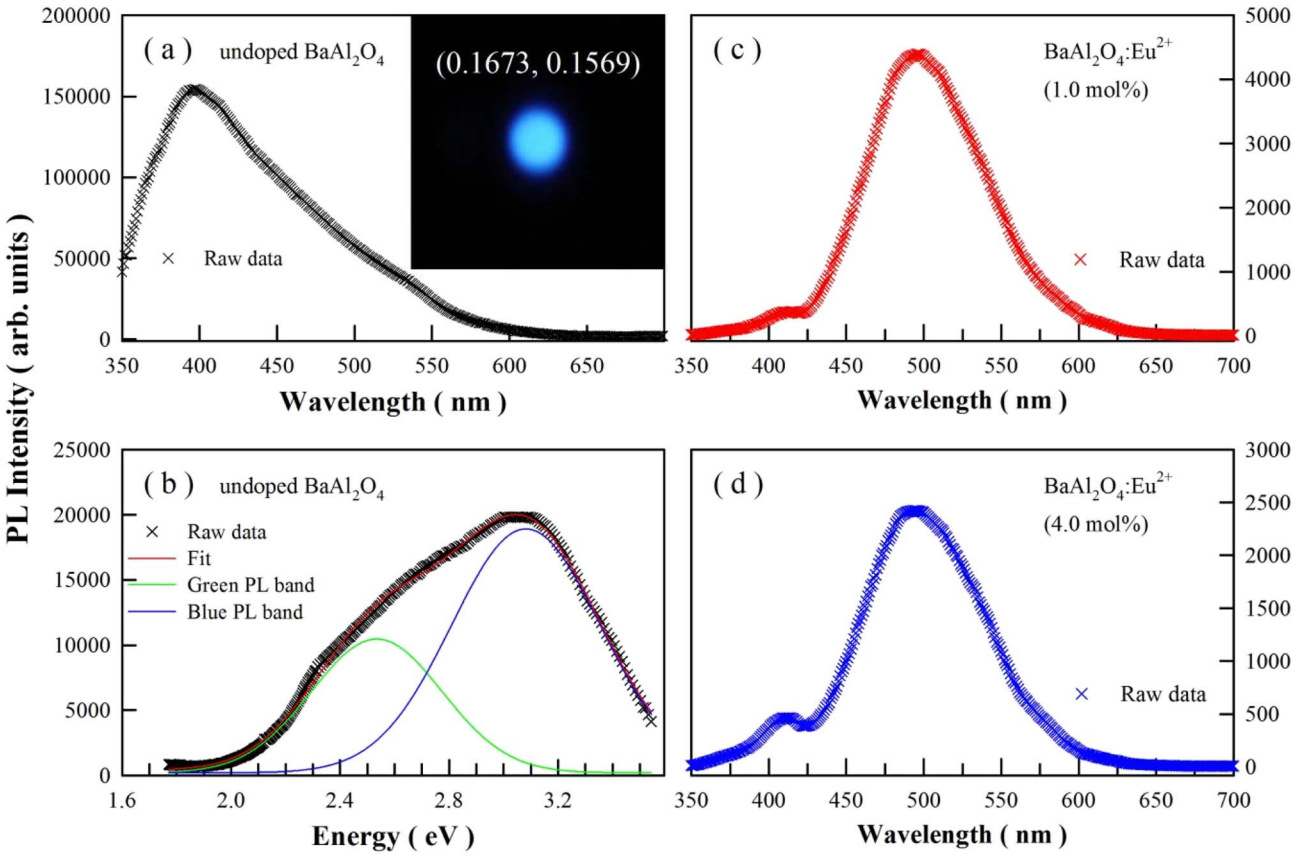

Fig. 6 (a) PL spectrum of undoped $BaAl_2O_4$ in wavelength scale; (b) PL spectrum of undoped $BaAl_2O_4$ in energy scale; (c) PL spectrum of Eu^{2+} doped $BaAl_2O_4$ (1.0 mol%) in wavelength scale; and (d) PL spectrum of Eu^{2+} doped $BaAl_2O_4$ (4.0 mol%) in wavelength scale. Inset in panel (a): PL photo of the phosphor under the 325 nm excitation.

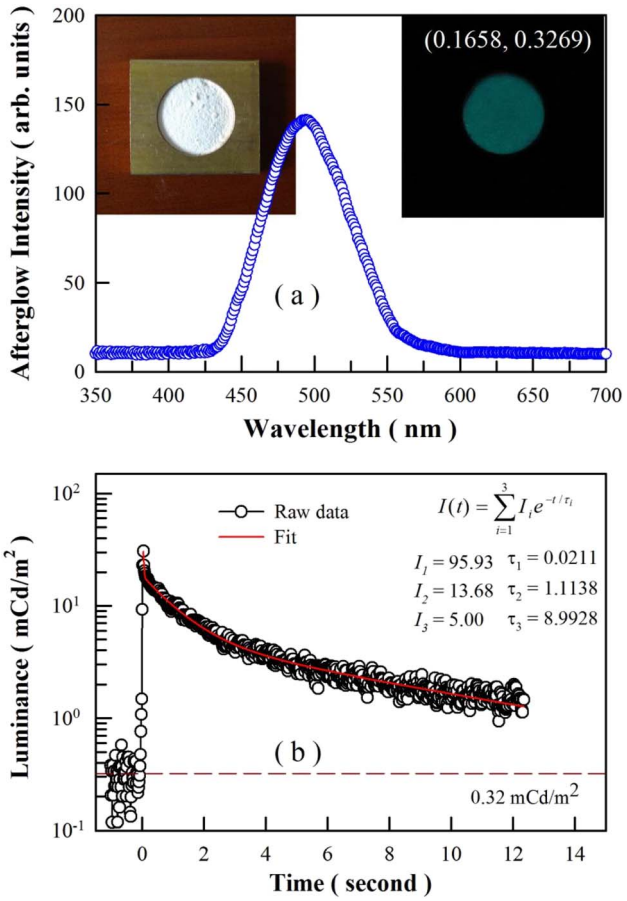

Fig. 7 Afterglow spectrum (a) and afterglow decay curve (b) of undoped $BaAl_2O_4$. Insets: the photograph of undoped $BaAl_2O_4$ under lab illumination (left) and the afterglow photograph of undoped $BaAl_2O_4$. The bronze sample holder is 20 mm in diameter.

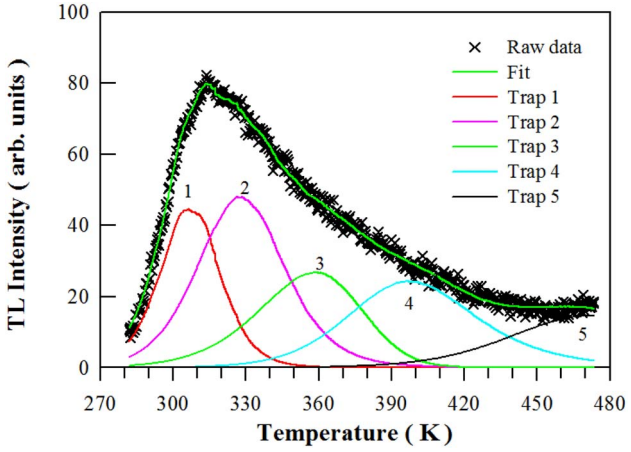

Fig. 8 Computerized deconvolution of the TL glow curve of undoped $BaAl_2O_4$.

profile and peak temperature of undoped $BaAl_2O_4$ are different from those of $BaAl_2O_4$:Eu^{2+},Re^{3+} because traps are sensitive to a number of factors such as sample preparation details, doping and irradiation.

Using a computer program given by Chung *et al.*,[58] we can deconvolute this TL glow curve with general order kinetics. As shown in Fig. 8, this TL glow curve is deconvoluted by assuming 5 traps in $BaAl_2O_4$. The kinetic parameters, figure-of-merit (FOM), and the electron lifetime at room temperature are listed in Table 1. The trap depths of the five traps in $BaAl_2O_4$ are determined to be 0.8589, 0.6738, 0.5450, 0.7097 and 0.7419 eV, respectively.

3.7. Electronic structures of defective $BaAl_2O_4$

The bluish-green afterglow and the blue PL of undoped $BaAl_2O_4$ seem to originate from the oxygen and barium vacancies in $BaAl_2O_4$. Our recent work demonstrates that the meta generalized gradient approximation can be utilized as an efficient exchange–correlation functional to calculate the band structures and DOS of $BaAl_2O_4$.[41] Fig. 9 represents the DFT calculated band structures and DOS of oxygen-deficient $BaAl_2O_4$: (a) the oxygen vacancy is the F^{2+} center; (b) the oxygen vacancy is the F^+ center; and (c) the oxygen vacancy is the F^0 center. The F^{2+}, F^+, and F^0 centers are doubly, singly, and neutrally charged oxygen vacancies, respectively. Before scissor operations, the calculated bandgap values of the F^{2+} bearing $BaAl_2O_4$, F^+ bearing $BaAl_2O_4$, and F^0 bearing $BaAl_2O_4$ are 6.064, 5.8675, and 6.0662 eV, respectively. These values are about 6.0, 9.3, and 6.2% less than the experimental value of $BaAl_2O_4$ (6.47 eV). After scissor operations, the bandgap of each oxygen-deficient $BaAl_2O_4$ is adjusted to be 6.47 eV. Correspondingly, the defect energy level of F^{2+} is located at 3.13 eV above the valence band maximum (VBM), the defect energy level of F^+ is located at 2.09 eV above VBM, and the defect energy levels of F^0 are located at 0.30, 4.69, 5.48, 5.63, and 6.26 eV above VBM. These defect energy levels provide abundant paths for optical absorption and emissions of undoped $BaAl_2O_4$. For instance, Zhang *et al.* recorded strong optical absorption in the spectral range 200–2500 nm in oxygen-deficient $BaAl_2O_4$.[59] Furthermore, both F^+ and F^{2+} centers are able to trap electrons from surrounding environment because they are positively charged. Therefore, oxygen vacancies might work as electron traps for afterglow.

The band structures and DOS of barium-deficient $BaAl_2O_4$ are also calculated. The defect energy levels of barium vacancy are found to locate at about 0.50 eV above VBM. This barium vacancy carries two negative charges. Being negatively charged, these barium vacancies might work as hole traps. Such traps capture holes easily in the valence band because they are very close to VBM. In an analogous DFT study of $SrAl_2O_4$, the defect energy levels of Sr vacancies are within 1 eV above VBM or even lie below VBM.[27] In another DFT study, McKenna *et al.* reported that the charge transition levels of hafnium vacancy in HfO_2 are 0.76–1.67 eV above VBM.[60]

3.8. Afterglow origins of undoped $BaAl_2O_4$

Among the three kinds of F centers, the defect energy levels of F^{2+} center are suitable for the blue emissions of undoped $BaAl_2O_4$. In light of the defect energy levels of the F^{2+} center and the barium vacancy, the processes of photo-excitation (process ①), carrier relaxation (process ②), carrier trapping (process ③),

Table 1 Kinetic parameters of the computerized deconvolution of the TL glow curve of undoped $BaAl_2O_4$. T_m represents the peak temperature, E is the trap-depth, s is the frequency factor, b is the order of kinetics, and τ_{300} is the room temperature electron lifetime in the trap

	T_m (K)	E (eV)	s (s^{-1})	b	n_0 (cm^{-3})	τ_{300} (h)	FOM (%)
Trap 1	306.35	0.8589	4.051×10^{11}	1.694	4.175×10^4	1.87×10^0	3.283
Trap 2	326.25	0.6738	5.136×10^7	1.747	6.659×10^4	1.08×10^1	
Trap 3	358.75	0.5450	7.399×10^4	1.191	4.362×10^4	1.36×10^1	
Trap 4	396.75	0.7097	1.624×10^6	2.000	5.137×10^4	3.65×10^4	
Trap 5	472.05	0.7419	9.745×10^4	2.000	4.163×10^4	2.20×10^6	

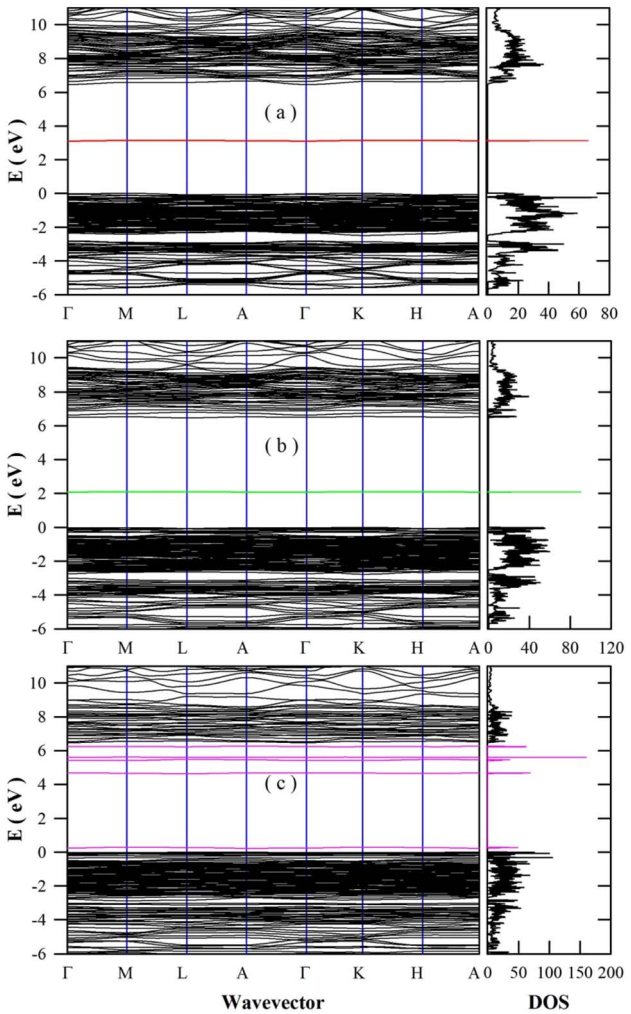

Fig. 9 DFT calculated band structures and DOS of oxygen-deficient $BaAl_2O_4$: (a) the oxygen vacancy is F^{2+} center; (b) the oxygen vacancy is F^+ center; and (c) the oxygen vacancy is F^0 center.

carrier detrapping (process ⑥), and carrier recombination (process ④ and ⑤) are sketched in Fig. 10 for undoped $BaAl_2O_4$. Detailed interpretations on the processes are available elsewhere.[19,20,22] Under the assumptions of the defect energy levels at E_V + 3.11 eV (for F^{2+} center) and E_V + 0.5 eV (for the barium vacancy), both the PL and the afterglow of undoped $BaAl_2O_4$ can be interpreted. If the mechanism in Fig. 10 sounds, we can expect that: (i) the PL spectrum of undoped $BaAl_2O_4$ would have one PL band peaking at about 3.13 eV (396 nm) and another PL band peaking at about 2.63 eV (472 nm); and (ii) the afterglow spectrum of undoped $BaAl_2O_4$ would be peaked at 2.63 eV (472 nm). Indeed, Fig. 6 verifies that the PL spectrum of undoped $BaAl_2O_4$ can be deconvoluted into a blue PL band centered at about 3.08 eV (402.6 nm) and a bluish-green PL band centered at 2.53 eV (490.1 nm). Furthermore, Fig. 7 confirms that the afterglow spectrum of undoped $BaAl_2O_4$ is peaked at about 2.51 eV (495 nm). The errors between the experimental and the expected data are related to the limited accuracy of the DFT calculations.

As illustrated in Fig. 10, there are two radiative relaxation paths, which are represented by processes ④ and ⑤, respectively. The radiative relaxation process ⑤ is evidenced by the broadband bluish green afterglow of undoped $BaAl_2O_4$ peaking at about 495 nm (2.51 eV). Conversely, the radiative relaxation process ④ is not evident in the afterglow spectrum of undoped $BaAl_2O_4$ because of the absence of a blue emission band peaking at about 3.08 eV (402.6 nm). Theoretically speaking, a blue emission band peaking at about 400 nm should coexist with the bluish-green emission band in the afterglow spectrum of undoped $BaAl_2O_4$ if the afterglow mechanism illustrated in Fig. 10 is correct. As discussed in our previous work, a hole at the energy level of barium vacancy has a lower energy than a hole in the valence band, thus holes tend to fill the energy level of barium vacancy at a much higher probability than holes occupy the valence band, which renders the contribution of process ④ negligible when compared to the process ⑤. This

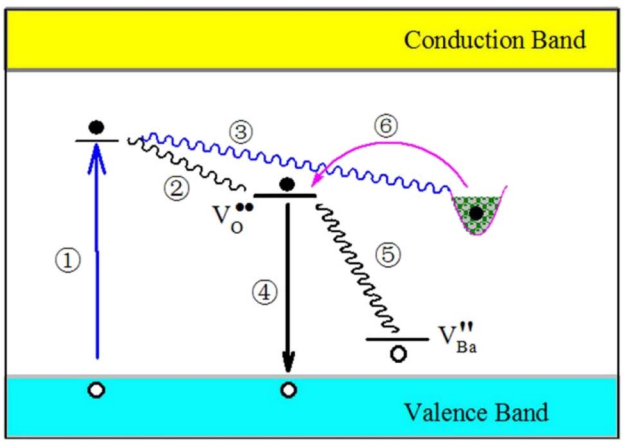

Fig. 10 Schematic illustration of the PL and afterglow mechanisms of undoped $BaAl_2O_4$. Details on the processes are available elsewhere.[19,20,22]

should be the reason why the afterglow spectrum of $BaAl_2O_4$ exhibits the bluish-green emission band only, leaving the blue emission band absent. This work focuses mainly on the PL and afterglow features of undoped $BaAl_2O_4$. It suggests that the presented mechanism of afterglow caused by vacancies may be regarded as just one of the afterglow sources in $BaAl_2O_4$:Eu^{2+} and $BaAl_2O_4$:Eu^{2+},Re^{3+}. In order to demonstrate without the doubt that Eu^{2+} is not an afterglow center in $BaAl_2O_4$:Eu^{2+} and $BaAl_2O_4$:Eu^{2+},Re^{3+}, comprehensive studies are highly necessary. Further work on the afterglow mechanisms of $BaAl_2O_4$:Eu^{2+} and $BaAl_2O_4$:Eu^{2+},Re^{3+} is on the way.

The $4f^6 5d \rightarrow 4f^7$ electric dipole transition of Eu^{2+} is parity-allowed, and the PL decay time of the transition in a large number of hosts is usually in the range from 0.2 to 2 μs. For example, the PL lifetime of $BaAl_2O_4$:Eu^{2+} was reported to be 0.9 μs at room temperature.[61] Therefore, the PL lifetime of undoped $BaAl_2O_4$ can provide complementary evidence on the intrinsic defects related emissions for undoped $BaAl_2O_4$. Fig. 11 illustrates the PL decays of undoped $BaAl_2O_4$ (black open circles) and their exponential reconvolutions (green solid curve) when the detection wavelengths are fixed at 400 nm (a) and 495 nm (b), respectively. The excitation wavelength is 320 nm. The instrument response function (blue solid curve) is given for each decay curve. Both decay curves can be deconvoluted by a tri-exponential decay function. As listed in Fig. 11, the averaged lifetimes are 7.39 and 4.70 ns for the emissions at 400 and 495 nm, respectively. These PL lifetimes are far shorter than that of $BaAl_2O_4$:Eu^{2+}, but are in line with those of the defect-related emissions in undoped $SrAl_2O_4$,[19] undoped $CaAl_2O_4$,[20] Eu^{2+} doped $CaAl_2O_4$,[22] and a large number of other inorganic materials.[29,42,53] The PL lifetimes in the order of a few nanoseconds reveal the nature of defect emissions of the two PL subbands of undoped $BaAl_2O_4$. In order to check whether undoped $BaAl_2O_4$ has longer PL lifetime, we have measured a series of PL decay curves of undoped $BaAl_2O_4$ by extending the pulsed period from 200 ns to 50 microsecond. PL lifetime longer than 10 ns, however, is not detected for undoped $BaAl_2O_4$. Alternatively, we measured a series of PL decay curves of Eu^{2+} doped $BaAl_2O_4$ (1.0 and 4.0 mol%) by extending the pulsed period from 50 ns to 50 microsecond. Analysis of the PL decay curves shows that PL lifetimes of Eu^{2+} doped $BaAl_2O_4$ (1.0 and 4.0 mol%) are less than 10 ns. It confirms that the PL lifetime of undoped $BaAl_2O_4$ is much shorter than 0.9 microsecond.

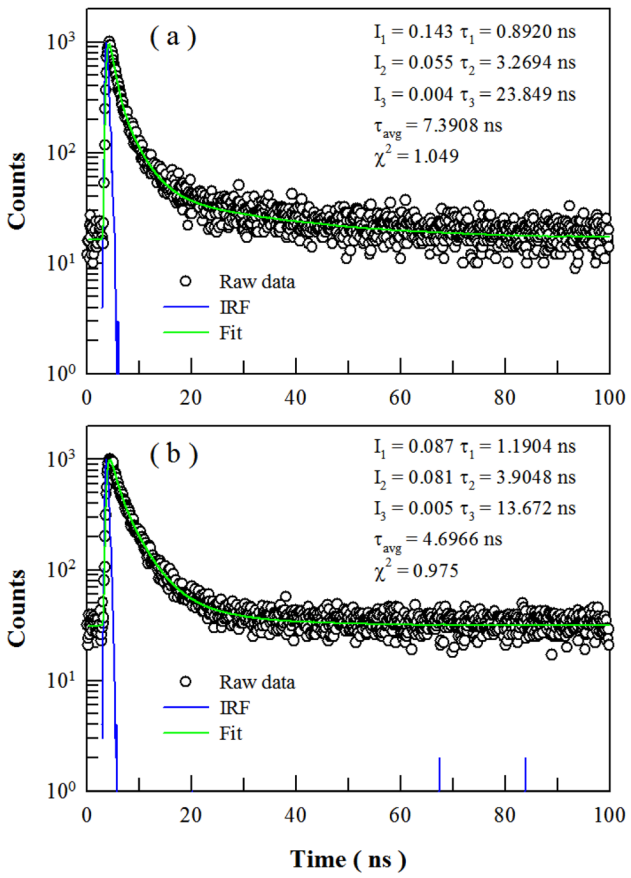

Fig. 11 PL decays (black open circles) and exponential reconvolution fits (green solid curves) of $BaAl_2O_4$ at different detection wavelengths: (a) 400 nm; and (b) 495 nm. Excitation wavelength: 320 nm. Pulsed period: 100 ns.

4. Conclusion

The afterglow and PL properties of sol–gel derived $BaAl_2O_4$ have been investigated. After excited by a high-pressure Hg lamp for 3 min, bluish-green afterglow of undoped $BaAl_2O_4$ is discernible to naked eye for about 20 s. The afterglow spectrum of the sol–gel derived $BaAl_2O_4$ has a broad profile with its peak at around 495 nm. The steady-state PL spectrum of the sol–gel derived $BaAl_2O_4$ can be deconvoluted into a bluish-green PL band centered at about 490.1 nm (2.53 eV) and a blue PL band centered at about 402.6 nm (3.08 eV). The TL glow curve reveals that a set of traps are present in undoped $BaAl_2O_4$. With their trap depths in the range of 0.5450–0.8589 eV. Defect energy levels of oxygen vacancies (*i.e.*, F^0, F^+ and F^{2+}) and doubly negatively charged calcium vacancy are derived *via* the DFT calculations. It is found that: (i) the defect energy level of F^{2+} center is located at 3.13 eV above VBM; (ii) the defect energy level introduced by the doubly negatively charged barium vacancy is about 0.5 eV above VBM; and (iii) the oxygen and calcium vacancies in undoped $BaAl_2O_4$ are the origin of the bluish-green afterglow and the blue PL of undoped $BaAl_2O_4$. Both the bluish-green afterglow and the blue PL of undoped $BaAl_2O_4$ can be interpreted in terms of defect energy levels introduced by the oxygen vacancy F^{2+} center and calcium vacancy. The recorded bluish-green afterglow of undoped $BaAl_2O_4$ is important to understand the afterglow mechanisms of rare-earth doped $BaAl_2O_4$.

Author contributions

B.-G. Z. synthesized the materials and wrote the initial drafts. Y. M. H. designed the experiments and supervised this work. All authors have read and agreed to the published version of the manuscript.

Conflicts of interest

There are no conflicts of interest to declare.

Acknowledgements

Financial support from National Natural Science Foundation of China (no. 11574036) was acknowledged.

References

1 T. Matsuzawa, Y. Aoki, N. Takeuchi and Y. Murayama, A new long phosphorescent phosphor with high brightness, $SrAl_2O_4$:Eu^{2+},Dy^{3+}, *J. Electrochem. Soc.*, 1996, **143**, 2670–2673.

2 L. C. V. Rodrigues, J. Hölsä, J. M. Carvalho, C. C. S. Pedroso, M. Lastusaari, M. C. F. C. Felinto, S. Watanabe and H. F. Brito, Co-dopant influence on the persistent luminescence of $BaAl_2O_4$:Eu^{2+},R^{3+}, *Phys. B*, 2014, **439**, 67–71.

3 D. B. Bem, F. B. Dejene, A. S. Luyt and H. C. Swart, Luminescence studies of a combustion-synthesized blue–green $BaAl_xO_y$:Eu^{2+},Dy^{3+} nanoparticles, *Phys. B*, 2012, **407**, 1561–1565.

4 M. A. Lephoto, O. M. Ntwaeaborwa, S. S. Pitale, H. C. Swart, J. R. Botha and B. M. Mothudi, Synthesis and characterization of $BaAl_2O_4$:Eu^{2+} co-doped with different rare earth ions, *Phys. B*, 2012, **407**, 1603–1606.

5 R. Sakai, T. Katsumata, S. Komuro and T. Morikawa, Effect of composition on the phosphorescence from $BaAl_2O_4$: Eu^{2+}, Dy^{3+} crystals, *J. Lumin.*, 1999, **85**, 149–154.

6 M. Malkamaki, A. J. J. Bos, P. Dorenbos, M. Lastusaari, L. C. V. Rodrigues, H. C. Swart and J. Holsa, Persistent luminescence excitation spectroscopy of $BaAl_2O_4$:Eu^{2+},Dy^{3+}, *Phys. B*, 2020, **593**, 411947.

7 B. G. Zhai, Q. L. Ma, R. Xiong, X. Li and Y. M. Huang, Blue–green afterglow of $BaAl_2O_4$:Dy^{3+} phosphors, *Mater. Res. Bull.*, 2016, **75**, 1–6.

8 R. Stefani, L. C. V. Rodrigues, C. A. A. Carvalho, M. C. F. C. Felinto, H. F. Brito, M. Lastusaari and J. Hölsä, Persistent luminescence of Eu^{2+} and Dy^{3+} doped barium aluminate ($BaAl_2O_4$:Eu^{2+},Dy^{3+}) materials, *Opt. Mater.*, 2009, **31**, 1815–1818.

9 H.-S. Roh, I.-S. Cho, J.-S. An, C. M. Cho, T. H. Noh, D. K. Yim, D.-W. Kim and K. S. Hong, Enhanced photoluminescence property of Dy^{3+} co-doped $BaAl_2O_4$:Eu^{2+} green phosphors, *Ceram. Int.*, 2012, **38**, 443–447.

10 H. Aizawa, S. Komuro, T. Katsumata, S. Sato and T. Morikawa, Long afterglow phosphorescent characteristics of $BaAl_2O_4$:Eu,Dy films, *Thin Solid Films*, 2006, **496**, 179–182.

11 D. den Engelsen, G. R. Fern, T. G. Ireland, F. Yang and J. Silver, Photoluminescence and cathodoluminescence of $BaAl_2O_4$:Eu^{2+} and undoped $BaAl_2O_4$: evidence for F-centres, *Opt. Mater. Express*, 2020, **10**, 1962–1980.

12 M. Ziyauddin, N. Brahme and A. K. Shrivastava, Luminescence properties of $BaAl_2O_4$:Eu^{2+} phosphors, *Int. Res. J. Eng. Technol.*, 2018, **5**, 3656–3660.

13 F. B. Dejene and M. A. Kebede, Synthesis and characterization of structural and luminescence properties of blue-green $BaAl_xO_y$:Eu^{2+} phosphor by solution – combustion method, *Cent. Eur. J. Phys.*, 2012, **10**, 977–982.

14 V. Ponnusamy, A. Azhagiri, R. Satheesh Kumar and M. T. Jose, Synthesis and role of co-dopants (alkaline earth divalents and halides) on the photoluminescence of Eu^{2+} doped $BaAl_2O_4$ phosphor, *Adv. Mater. Lett.*, 2019, **10**, 341–345.

15 Y. Li, M. Gecevicius and J. Qiu, Long persistent phosphors-from fundamentals to applications, *Chem. Soc. Rev.*, 2016, **45**, 2090.

16 T. Aitasalo, P. Dereń, J. Hölsä, H. Jungner, J. C. Krupa, M. Lastusaari, J. Legendziewicz, J. Niittykoski and W. J. Stręk, Persistent luminescence phenomena in materials doped with rare earth ions, *J. Solid State Chem.*, 2003, **171**, 114–122.

17 P. Dorenbos, Mechanism of persistent luminescence in Eu^{2+} and Dy^{3+} codoped aluminate and silicate compounds, *J. Electrochem. Soc.*, 2005, **152**, H107–H110.

18 F. Clabau, X. Rocquefelte, S. Jobic, P. Deniard, M. H. Whangbo, A. Garcia and T. Le Mercier, Mechanism of phosphorescence appropriate for the long-lasting phosphors Eu^{2+}-doped $SrAl_2O_4$ with codopants Dy^{3+} and B^{3+}, *Chem. Mater.*, 2005, **17**, 3904–3912.

19 B. G. Zhai and Y. M. Huang, Green afterglow of undoped $SrAl_2O_4$, *Nanomater.*, 2021, **11**, 2331.

20 B. G. Zhai and Y. M. Huang, Blue afterglow of undoped $CaAl_2O_4$ nanocrystals, *Europhys. Lett.*, 2019, **127**, 17001.

21 B. G. Zhai, H. Xu, F. Zhuo and Y. M. Huang, Annealing temperature dependent photoluminescence and afterglow of undoped $CaAl_2O_4$, *J. Alloys Compd.*, 2020, **821**, 153563.

22 B. G. Zhai and Y. M. Huang, Doping concentration dependent photoluminescence and afterglow of Eu^{2+} doped $CaAl_2O_4$ for insight into the afterglow mechanisms, *Phys. B*, 2022, **646**, 414284.

23 Y. M. Huang and Q. L. Ma, Long afterglow of trivalent dysprosium doped strontium aluminate, *J. Lumin.*, 2015, **160**, 271–275.

24 B. G. Zhai, L. Yang, Q. L. Ma, X. Liu and Y. M. Huang, Mechanism of the prolongation of the green afterglow of $SrAl_2O_4$:Dy^{3+} caused by the use of H_3BO_3 flux, *J. Lumin.*, 2017, **181**, 78–87.

25 Q. L. Ma, B. G. Zhai and Y. M. Huang, Effect of sol-gel combustion temperature on the luminescent properties of trivalent Dy doped $SrAl_2O_4$, *Ceram. Int.*, 2015, **41**, 5830–5835.

26 B. G. Zhai and Y. M. Huang, Green photoluminescence and afterglow of Tb doped $SrAl_2O_4$, *J. Mater. Sci.*, 2017, **52**, 1813–1822.

27 E. Finley, A. M. Tehrani and J. Brgoch, Intrinsic defects drive persistent luminescence in monoclinic $SrAl_2O_4$:Eu^{2+}, *J. Phys. Chem. C*, 2018, **122**, 16309–16314.

28 D. A. Pejakovic, Studies of the phosphorescence of polycrystalline hafnia, *J. Lumin.*, 2010, **130**, 1048–1054.

29 B. G. Zhai, H. Xu, Q. Zhang and Y. M. Huang, Blue photoluminescence and cyan-colored afterglow of undoped $SrSO_4$ nanoplates, *ACS Omega*, 2021, **6**, 10129–10140.

30 Z. Zhou, K. Jiang, N. Chen, Z. Xie, B. Lei, J. Zhuang, X. Zhang, Y. Liu and C. Hu, Room temperature long afterglow from boron oxide: A boric acid calcined product, *Mater. Lett.*, 2020, **276**, 128226.

31 K. Iwasaki, Y. Takahashi, N. Terakado, N. Onoue, T. Shinozaki and T. Fujiwa, Prominent long-lasting photoluminescence in defect-activated zirconia: A rare-earth free and accessible phosphor, *Ceram. Int.*, 2018, **44**, 12929–12933.

32 B. G. Zhai, H. Xu and Y. M. Huang, Annealing temperature dependent afterglow of Tb^{3+} doped $CaAl_2O_4$, *Opt. Mater.*, 2021, **112**, 110739.

33 B. G. Zhai and Y. M. Huang, Extending the afterglow of Tb^{3+} doped $CaAl_2O_4$ to 8 hours via the control of doping concentration, *J. Lumin.*, 2022, **244**, 118725.

34 B. G. Zhai, L. Yang, F. F. Zhou, J. S. Shi and Y. M. Huang, Strong photo-oxidative capability of $ZnWO_4$ nanoplates with highly exposed {0-11} facets, *Catalysts*, 2019, **9**, 178.

35 Y. M. Huang, M. Y. Li, L. Yang and B. G. Zhai, Eu^{2+} and Eu^{3+} doubly doped $ZnWO_4$ nanoplates with superior photocatalytic performance for dye degradation, *Nanomater.*, 2018, **8**, 765.

36 N. Yamashita, T. Hamada, M. Takada, M. Katsuki and M. Nakagawa, Photoluminescence and thermoluminescence of $MgSO_4$, $CaSO_4$, $SrSO_4$ and $BaSO_4$ powder phosphors activated with Tb^{3+}, *Jpn. J. Appl. Phys.*, 2001, **40**, 6732–6736.

37 B. G. Zhai, M. M. Chen and Y. M. Huang, Photoluminescence and afterglow of Dy^{3+} doped $CaAl_2O_4$ derived via sol–gel combustion, *RSC Adv.*, 2022, **12**, 31757.

38 A. D. Becke and E. R. Johnson, A simple effective potential for exchange, *J. Chem. Phys.*, 2006, **124**, 221101–221104.

39 F. Tran and P. Blaha, Accurate band gaps of semiconductors and insulators with a semilocal exchange-correlation potential, *Phys. Rev. Lett.*, 2009, **102**, 226401.

40 D. Koller, F. Tran and P. Blaha, Merits and limits of the modified Becke-Johnson exchange potential, *Phys. Rev. B: Condens. Matter Mater. Phys.*, 2011, **83**, 195134.

41 B. G. Zhai and Y. M. Huang, First-principles calculations of hexagonal $BaAl_2O_4$, *Solid State Commun.*, 2023, **362**, 115101.

42 B. G. Zhai, L. Yang, Q. L. Ma and Y. M. Huang, Visible light driven photocatalytic activity of Fe-doped ZnO nanocrystals, *Funct. Mater. Lett.*, 2017, **10**, 1750002.

43 L. L. Chen, B. G. Zhai and Y. M. Huang, Rendering visible-light photocatalytic activity to undoped ZnO via intrinsic defects engineering, *Catalysts*, 2020, **10**, 1163.

44 R. Chatterjee, S. Saha, K. Panigrahi, U. K. Ghorai, G. C. Das and K. K. Chattopadhyay, Blue emitting $BaAl_2O_4:Ce^{3+}$ nanophosphors with high color purity and brightness for white LEDs, *Microsc. Microanal.*, 2019, **25**, 1466–1470.

45 J. Mooney and P. Kambhampati, Get the basics right: Jacobian conversion of wavelength and energy scales for quantitative analysis of emission spectra, *J. Phys. Chem. Lett.*, 2013, **4**, 3316–3318.

46 V. Chernov, T. M. Piters, R. Ruiz-Torres, P. Salas-Castillo, N. J. Zuñiga-Rivera, R. Meléndrez and M. Barboza-Flores, Effect of reducing and oxidizing atmosphere on photoluminescence of undoped and Eu doped nanostructured $CaAl_2O_4$, *J. Lumin.*, 2022, **251**, 119196.

47 Q. L. Ma, R. Xiong and Y. M. Huang, Tunable photoluminescence of porous silicon by liquid crystal infiltration, *J. Lumin.*, 2011, **131**, 2053–2057.

48 Q. L. Ma, B. G. Zhai and Y. M. Huang, Sol–gel derived ZnO/porous silicon composites for tunable photoluminescence, *J. Sol-Gel Sci. Technol.*, 2012, **64**, 110–116.

49 B. G. Zhai, Q. L. Ma, L. Yang and Y. M. Huang, Synthesis and optical properties of Tb-doped pentazinc dimolybdate pentahydrate, *Results Phys.*, 2017, **7**, 3991–4000.

50 L. C. V. Rodrigues, R. Stefani, H. F. Brito, M. C. F. C. Felinto, J. Holsa, M. Lastusaari, T. Laamanen and M. Malkamaki, Thermoluminescence and synchrotron radiation studies on the persistent luminescence of $BaAl_2O_4:Eu^{2+},Dy^{3+}$, *J. Solid State Chem.*, 2010, **183**, 2365–2371.

51 B. G. Zhai, D. Liu, Y. He, L. Yang and Y. M. Huang, Tuning the photoluminescence of Eu^{2+} and Eu^{3+} co-doped $SrSO_4$ through post annealing technique, *J. Lumin.*, 2018, **194**, 485–493.

52 V. A. Gritsenko, D. R. Islamov, T. V. Perevalov, V. Sh. Aliev, A. P. Yelisseyev, E. E. Lomonova, V. A. Pustovarov and A. Chin, Oxygen vacancy in hafnia as a blue luminescence center and a trap of charge carriers, *J. Phys. Chem. C*, 2016, **120**, 19980–19986.

53 B. G. Zhai, L. Yang and Y. M. Huang, Intrinsic defect engineering in Eu^{3+} doped $ZnWO_4$ for annealing temperature tunable photoluminescence, *Nanomater.*, 2019, **9**, 99.

54 B. G. Zhai, L. Yang, Q. L. Ma and Y. M. Huang, Growth of $ZnMoO_4$ nanowires via vapor deposition in air, *Mater. Lett.*, 2017, **188**, 119–122.

55 B. G. Zhai, Q. L. Ma, L. Yang and Y. M. Huang, Effects of sintering temperature on the morphology and photoluminescence of Eu^{3+} doped zinc molybdenum oxide hydrate, *J. Nanomater.*, 2018, **2018**, 7418508.

56 R. K. Gartia and M. N. Singh, Deconvolution of thermoluminescence curves and its implications: The case of $CaAl_2O_4:Sm^{3+}$, *Optik*, 2021, **248**, 168048.

57 A. Pandey and M. L. Chithambo, Thermoluminescence of the persistent-luminescence phosphor, $BaAl_2O_4$; A stuffed tridymite, *Radiat. Meas.*, 2018, **120**, 73–77.

58 K. S. Chung, J. I. Lee and J. L. Kim, A computer program for the deconvolution of the thermoluminescence glow curves by employing the interactive trap model, *Radiat. Meas.*, 2012, **47**, 766–769.

59 L.-W. Zhang, L. Wang and Y.-F. Zhu, Synthesis and performance of $BaAl_2O_4$ with a wide spectral range of optical absorption, *Adv. Funct. Mater.*, 2007, **17**, 3781–3790.

60 K. P. McKenna and D. M. Ramo, Electronic and magnetic properties of the cation vacancy defect in *m*-HfO_2, *Phys. Rev. B: Condens. Matter Mater. Phys.*, 2015, **92**, 205124.

61 S. H. M. Poort, A. Meyerink and G. Blasse, Lifetime measurements in Eu^{2+}-doped host lattices, *J. Phys. Chem. Solids*, 1997, **58**, 1451–1456.